

Inside-Outside Lithium Deposition Achieved by the Unusual Strategy of Constructing the Hierarchical Lithiophilicity for Dendrite-Free and Durable Lithium Metal Anode

Xiao-Meng Lu⁺^[a] Tiancun Liu⁺^[a, b] Yong Wang,^{*[a, c]} and Fei-Hu Du^{*[a]}

Uncontrollable dendritic lithium (Li) growth and huge volume fluctuation are critical issues for the commercialization of Li metal anode. This work reports a three-dimensional conductive host with hierarchical lithiophilicity to promote the uniform Li plating/stripping. Except for the common merits of the large surface area and excellent conductivity, the unique structural and compositional design, Ag nanoparticles encapsulated inside nitrogen-doped carbon hollow spheres (Ag@NCHSs), allows a model of inside-outside Li deposition due to the promising

lithiophilicity of Ag component. This type of Li deposition strategy is evidenced by *in-situ* optical microscope, *in-situ* X-ray diffraction (XRD) patterns and endows a promising ability to overcome the fatal issues of Li metal anode even at high areal capacities and current densities. As a result, the developed host with the hierarchical lithiophilicity enables a remarkable enhancement of cycling performances. The strategy of constructing hierarchical lithiophilicity brings new insights to stabilize the Li metal anode.

Introduction

Nowadays, lithium (Li)-ion battery (LIB) technology adopting graphite anode is changing society life, but its insufficient energy supply seems not to meet the energy density requirements of future large-scale transportation and electronic devices.^[1,2] Therefore, other advanced storage systems are expected to be explored. Rechargeable high-energy Li metal batteries (LMBs) with sulfur and oxygen cathodes provide a good chance to solve the issue. Li metal anode (LMA), as the one part of LMBs, possesses the unparalleled theoretical specific capacity of 3860 mAh g⁻¹ and ultralow electrochemical potential of -3.04 V versus standard hydrogen electrode.^[3–6] However, because of the high interfacial chemical reaction and hostless property of LMA, some persistent drawbacks are triggered, leading to the difficult realization of practical LMBs. Concretely, uncontrollable dendritic Li growth caused by uneven Li dispersion, formation of deactivated “dead Li” region,

huge volume fluctuation during the Li plating/stripping process and unnecessary electrolyte loss for constructing new solid electrolyte interface (SEI) are inevitable to lower the Coulombic efficiency (CE), reduce the capacity retention and even guide the internal short circuit.^[7–10] For decades, massive innovative efforts in tuning the uniform Li deposition/dissolution behavior have been conducted.^[11,12] Especially, modulating functional additive electrolytes,^[13–15] fabricating the solid-state electrolyte^[16–20] and constructing a chemically stable artificial protection layer^[21–24] have exhibited the positive effects on achieving stable LMA and optimizing the electrochemical performance of LMBs. Moreover, rationally designing a lithiophilic three-dimensional (3D) current collector is beneficial to inhibiting the generation of Li dendrite and improving the LMA.^[25–29]

Recently, Guo et al.^[18,19] have developed an outstanding 3D porous carbon material for LMA, showing improved electrochemical properties because of sufficient diffusion channels for Li ions and the accommodated huge volume variation. Unfortunately, it is difficult to regulate the Li ion concentration near the electrode interface, contributing to large nucleation overpotential and unsatisfied cyclability. Dendrite growth has not been fundamentally inhibited when Li deposition exceeds a certain capacity, eventually causing safety issues of the cell failure.^[30] Yan et al. reported a significant difference in Li metal nucleation potentials on different substrates, which offers a unique insight of spatially controlling Li deposition.^[31] This opens up a new approach to limit the growth of Li dendrites by selectively guiding Li deposition into 3D host decorated with heterogeneous lithiophilic sites. Impressively, Hu et al. reported a functional skeleton to guide uniform plating and avoid the formation of dendritic Li, on which plenty of ultrafine Ag nanoparticles anchored to form lithiophilic network.^[32]

[a] X.-M. Lu,⁺ Dr. T. Liu,⁺ Prof. Y. Wang, Dr. F.-H. Du
School of Environmental and Chemical Engineering
Shanghai University
99 Shangda Road, Shanghai 200444, China
E-mail: yongwang@shu.edu.cn
fh_du@shu.edu.cn

[b] Dr. T. Liu⁺
School of Materials Science and Engineering
Zhejiang Sci-Tech University
Hangzhou 310018, China

[c] Prof. Y. Wang
Key Laboratory of Organic Compound Pollution Control Engineering (MOE)
Shanghai University
99 Shangda Road, Shanghai 200444, China

[+] These authors contributed equally to this work.

Supporting information for this article is available on the WWW under
<https://doi.org/10.1002/batt.202200114>

Except for the successful operation of homogeneous Li nucleation and evolution, these plated Li metal could be only dispersed on the outer nanofiber surface of this lithiophilic skeleton, resulting in the unavoidable exposure to the electrolyte and subsequent excess electrolyte consumption. It can be expected that the rational design of 3D lithiophilic host with the function of protecting plated Li metal will be more important to achieve the dendrite-free LMA and high-performance LMBs.

Herein, an unusual substrate with the heterogeneous lithiophilicity, Ag nanoparticles encapsulated inside nitrogen (N)-doped carbon hollow spheres (denoted as Ag@NCHSs), is demonstrated to induce uniform Li deposition. For Ag@NCHSs, the structural and compositional design offers multiple advantages: 1) 3D conductive host material with mesopores and large surface area can increase the electron transfer rate and decrease local current density; 2) Li metal is prior to be nucleated on the filled Ag nanoparticles inside carbon spheres, following an inside-out model; 3) abundant internal space of the NCHSs can withstand huge volume change and confine Li growth; 4) N-doped carbon materials can endow a uniform distribution of Li ions, subsequently promoting the outer uniform Li deposition in the space among neighboring spheres. As applied in the current collector of LMA, Ag@NCHSs electrodes ensure remarkable electrochemical performances of the ultrahigh CE values, improved cycling stability and enhanced working lifespan. Moreover, dendrite-free Li deposition can be directly observed by *in-situ* optical microscopy. This rational skeleton design helps promote the development of preparing the multi-functional current collector for LMBs.

Results and Discussion

Schematic illustrations of Li nucleation and electroplating behavior on Ag@NCHSs, NCHSs and Cu foil substrate are shown in Figures 1(a), S1 and 1(b), respectively. For Ag@NCHSs (Figure 1a), benefiting from the synergistic effect of heterogeneous seeding and spatial confinement, the plated Li metal preferentially reacts with interior lithiophilic Ag nanoparticles to form Li–Ag alloy sites and then gradually fill the internal sphere cavity along these sites. As the internal deposition capacity limit is reached, subsequent Li metal plating continues to occur on the exterior spaces outside Ag@NCHSs spheres. Plenty of gaps or spaces among adjacent spheres will be smoothly submerged by Li metal in the following plating process, leading to a dendrite-free morphology. This shows that the constructed lithiophilic structure can control the structural evolution of Li deposition and promote the uniform migration of Li ions to the lithiophilic surface. In comparison, due to the poor lithiophilicity of the Cu foil with rough surface, randomly-distributed nucleation sites result in the development of irregular Li growth and eventual formation of large Li dendrites (Figure 1b). For common NCHSs (Figure S1), due to the decoration of lithiophilic N-containing sites, the migrated Li ions during Li plating process can cause preferential deposition on the exterior surface rather than the internal spaces of carbon spheres. The outer exposed Li metal is possible to consume excess electrolyte and accelerate the cell failure. Moreover, this behavior cannot exhibit the advantage of large loading amount of Li metal rendered by the hollow structure of NCHSs, causing the low utilization rate of internal large space.

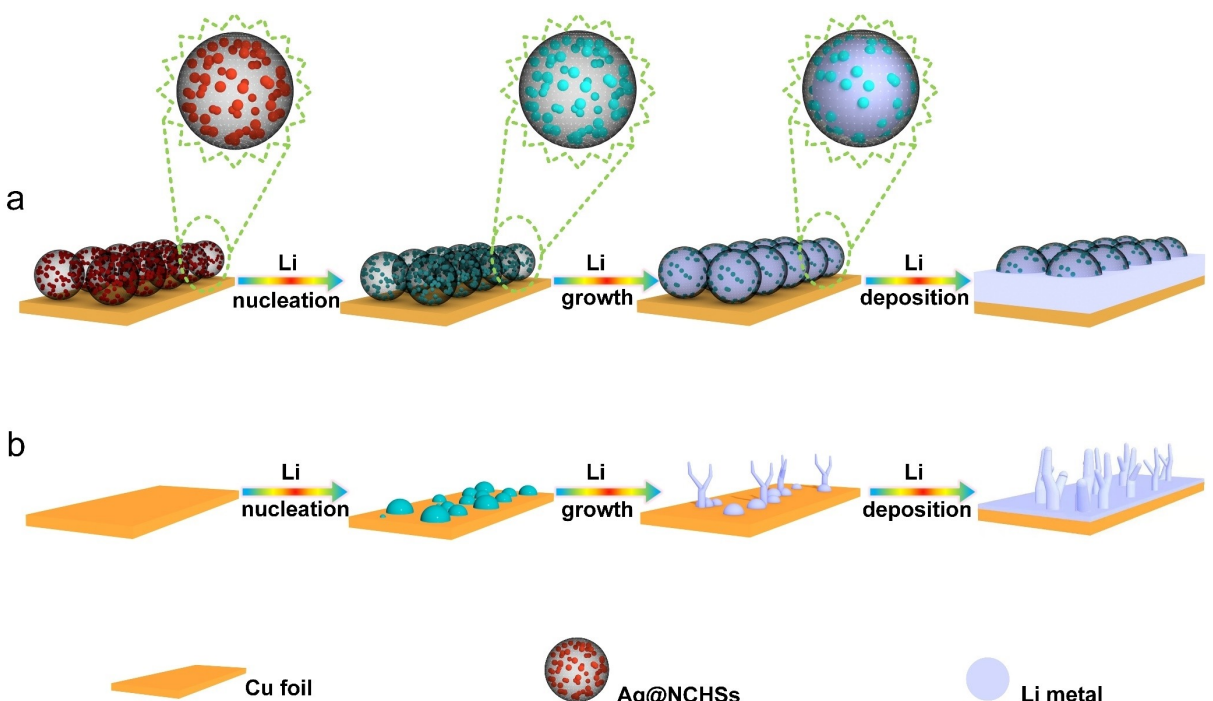


Figure 1. Schematic illustration of Li nucleation and electroplating behaviors on (a) Ag@NCHSs based substrate and (b) Cu foil.

The fabrication process of the Ag@NCHSs is schematically displayed in Figure 2(a). Firstly, mesoporous silica hollow spheres (MHSiO_2) were prepared by our previous work.^[33] Secondly, the decoration of Ag nanoparticles on the surface of MHSiO_2 ($\text{MHSiO}_2@\text{Ag}$) was conducted by a simple chemical reduction of AgNO_3 at a mild temperature. Thirdly, to obtain the nitrogen-doped graphene coating on the $\text{MHSiO}_2@\text{Ag}$ ($\text{MHSiO}_2@\text{Ag@NC}$), the as-prepared $\text{MHSiO}_2@\text{Ag}$ was processed by the chemical vapor deposition (CVD) method adopting acetonitrile as the carbon source. Finally, for the production of Ag@NCHSs, dilute HF was used to remove the internal MHSiO_2 template of $\text{MHSiO}_2@\text{Ag@NC}$. Scanning electron microscopy

(SEM) images of MHSiO_2 , NCHSs and Ag@NCHSs are shown in Figure 2(b-d), respectively. It could be clearly observed that there was no big appearance difference among three samples, indicating the excellent structure stability during the preparation process. To determine the unique characteristic of these three samples, transmission electron microscopy (TEM) images have been conducted and are displayed at Figure 2(e-g). For the MHSiO_2 material, typical hollow structure with a diameter of ~600 nm was observed in Figure 2(e). After the N-doped carbon coating and template etching process, NCHSs could stably maintain the hollow structure with a thin thickness (Figure 2f). This manifests the carbon coating possesses a

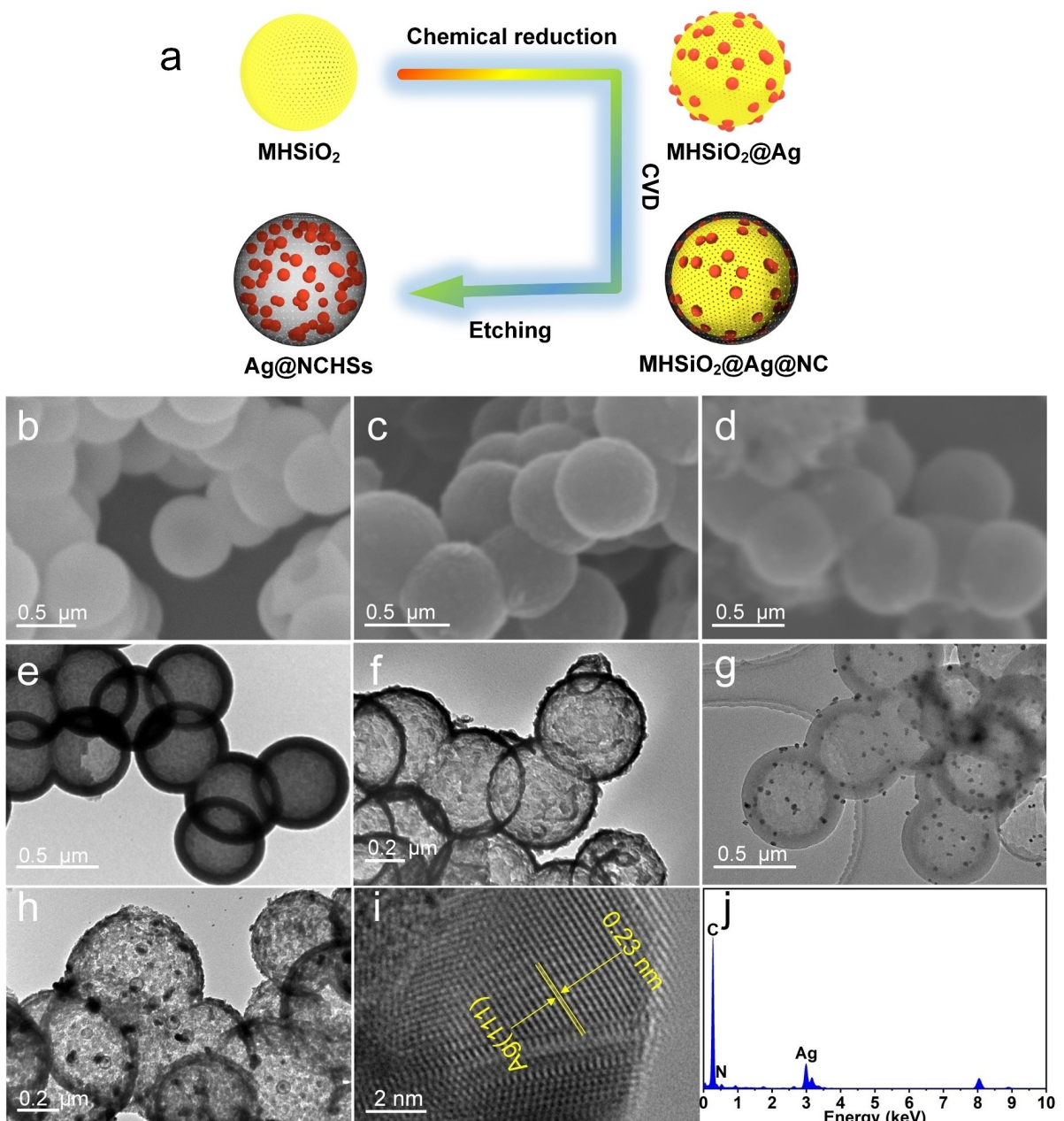


Figure 2. Fabrication strategy, morphology and structure of the products. a) Schematic illustration of the synthesis of Ag@NCHSs. SEM images of b) MHSiO_2 , c) NCHSs and d) Ag@NCHSs. TEM images of the e) MHSiO_2 , f) NCHSs, g) $\text{MHSiO}_2@\text{Ag}$ and h) Ag@NCHSs. i) High-resolution TEM image showing lattice fringes of the Ag Nanoparticles. j) The corresponding EDX result of C, N and Ag distribution in Ag@NCHSs.

superior mechanical property, endowing the large internal space. Figure 2(g) exhibits the TEM image of $\text{MHSiO}_2@\text{Ag}$ sample, from which the notable hierarchical structure and numerous Ag nanoparticles anchored on the surface of MHSiO_2 could be clearly observed. As shown in Figure 2(h), after removing the MHSiO_2 core, only some Ag nanoparticles are dispersed in the hollow carbon shell with the uniform hollow morphology and the decoration of Ag nanoparticles hardly affected the regular structure. As exhibited in the HRTEM image of the face-centered cubic Ag (Figure 2i), the lattice distance of 0.23 nm should be corresponded to the crystal plane (111) of the Ag phase (JCPDS 04-0783). The energy-dispersive X-ray (EDX) spectrum illustrated that Ag elements (mass loading: 23.5%) were presented in the final product (Figure 2j), proving the rational preparation of Ag@NCHSs. Moreover, thermal

gravimetric analysis (TGA) of Ag@NCHSs disclosed the weight content of Ag was measured about 21.1% (Figure S5), which was close to the EDX result.

The X-ray diffraction (XRD) patterns of the Ag@NCHSs and NCHSs are shown in Figure 3(a). Specially, three intense diffraction peaks at 38.2° , 44.4° and 64.6° were exhibited in Ag@NCHSs material, corresponding to the (111), (200), and (220) planes of the face-centered cubic Ag respectively. In contrast, there was only one small peak at $\sim 26^\circ$ in NCHSs. In addition to the broad peak at 23° of pure silica component, an additional diffraction peak at 38.2° could be noted in $\text{MHSiO}_2@\text{Ag}$, thus confirming the successful loading of Ag nanoparticles (Figure S2). Figure 3(b) displays the Raman spectra of Ag@NCHSs and NCHSs with the typical D and G bands of carbon. Compared to pristine NCHSs, the G band of Ag@NCHSs

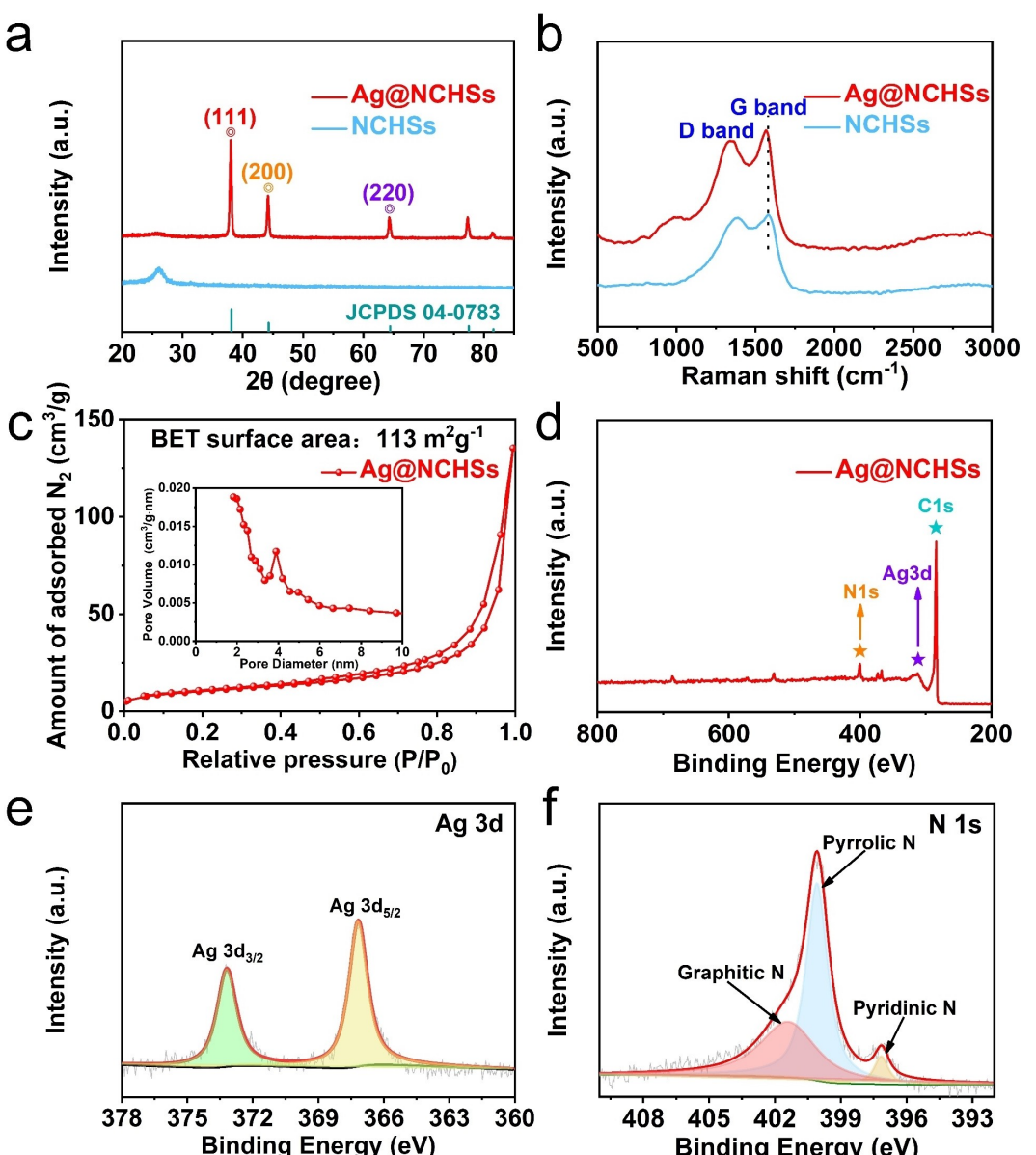


Figure 3. Characterization of the Ag@NCHSs and NCHSs materials. a) XRD patterns and b) Raman spectra of the NCHSs and Ag@NCHSs powders. c) N_2 adsorption and desorption isotherms of Ag@NCHSs. d) XPS full survey spectrum of the Ag@NCHSs. High-resolution XPS spectra of e) Ag 3d and f) N 1s.

delivered an imperceptible red shift from 1566 to 1581 cm⁻¹, further indicating the presence of metallic Ag nanoparticles.^[34,35] Typical mesoporous structure (2.8 nm in diameter) and high specific surface area (SSA) of 1047 m² g⁻¹ of MHSiO₂ could be obtained from nitrogen adsorption-desorption isotherm (Figure S3). The extremely large SSA of MHSiO₂ should be provided by abundant pores in the structure. After the removal of MHSiO₂, there were low SSA values of 113 and 141.9 m² g⁻¹ for Ag@NCHSs and NCHSs (Figures 3c and S4). Particularly, heavy weight of loaded Ag component in Ag@NCHSs is inevitable to decrease the SSA, compared to that of NCHSs. X-ray photoelectron spectroscopy (XPS) was applied to evaluate the chemical composition and valence state analysis for Ag@NCHSs, in which N, C and Ag elements could be detected (Figure 3d). In the high-resolution Ag 3d spectrum, there were two individual characteristic peaks located at 367.1 and 373.2 eV, which should be assigned to Ag 3d_{5/2} and Ag 3d_{3/2},

, respectively (Figure 3e). Figure 3(f) exhibits the high-resolution N 1s spectrum, three kinds of N-containing groups were located at 397.1, 400.1 and 401.4 eV, corresponding to pyridinic N, pyrrolic N and graphitic N respectively. The co-existence of lithiophilic Ag and N-containing groups (pyridinic N and pyrrolic N) may show a synergistic effect on guiding uniform Li deposition.

To determine the Li deposition behavior in the Ag@NCHSs and NCHSs (denoted as Ag@NCHSs@Li and NCHSs@Li), the morphology variation of two substrates with various areal capacities of Li metal was inspected. Figure 4(a-c) shows the morphology evolution of Li metal on Ag@NCHSs at various deposition capacities from 0 to 3 mAh cm⁻². Before Li plating, clear and regular structure outline of the prepared Ag@NCHSs could be observed (Figure 4a). When the Li plating capacity was 1 mAh cm⁻², Ag@NCHSs was able to maintain the sphere-like morphology well (Figure 4b), resulting from the prior

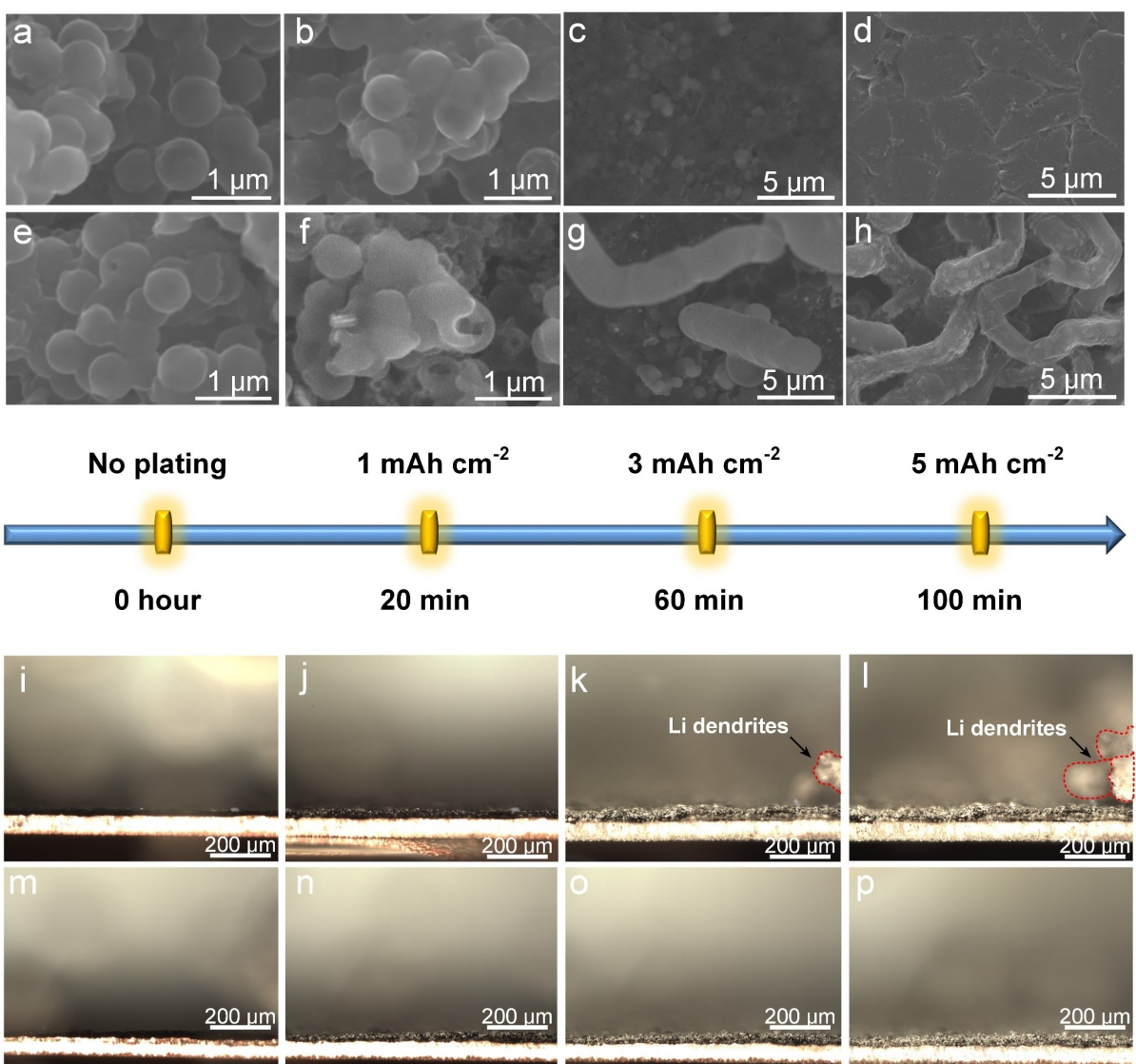


Figure 4. Li metal deposition behaviors on Ag@NCHSs and NCHSs. SEM images of a-d) Ag@NCHSs and e-h) NCHSs electrodes after Li plating a and e) 0, b and f) 1, c and g) 3, d and h) 5 mAh cm⁻² at a current density of 1 mA cm⁻². i–p) In-situ optical microscopy observation on Li deposition of i–l) NCHSs and m–p) Ag@NCHSs at a current density of 3 mA cm⁻² in relation to the discharge time of i and m) 0, j and n) 20, k and o) 60, l and p) 100 min.

internal Li deposition and growth. Meanwhile, the phenomenon of slightly filled gaps among spheres should be noticed, indicating the outside Li deposition started to occur. This is because of the preferential inside Li nucleation and growth induced by the formed Ag–Li alloy, following the uniform outside Li plating caused by N-doped groups.^[36] As shown in Figure 4(c), Ag@NCHSs was disappeared after Li plating of 3 mAh cm^{-2} . Benefiting from the early homogeneous induction of Li deposition, the electrode exhibited a flat surface and dense deposition, demonstrating Li filled up the outside void space. Even a large amount of metallic Li (5 mAh cm^{-2}) was transferred in the substrate, dense distribution of Li metal and no dendrite formation could be determined, indicating the excellent ability to disperse Li ions due to the lithophilic sites (Figure 4d). Moreover, to prove the unique inside-outside Li deposition, the morphology variations of Ag@NCHSs with various deposition capacities have been also characterized by TEM. Figure S7(a) shows some Ag nanoparticles and hollow morphology of Ag@NCHSs before Li plating. When the Li plating capacity was 0.3 mAh cm^{-2} , Ag nanoparticles slightly expanded due to the alloying reaction, and Li metal was deposited near these sites (Figure S7b). Gradually, as the capacity increased to 0.5 mAh cm^{-2} , the internal space was mostly occupied (Figure S7c). Afterwards, as displayed in Figure S7(d), it is noteworthy that Ag@NCHSs would be covered by more deposited Li of 1 mAh cm^{-2} , because the internal void has been fully filled up. The morphology variation of Ag@NCHSs with Li metal helps manifest the unique inside-outside Li deposition. Observed from these SEM and TEM images of Ag@NCHSs@Li electrodes, the superior synergistic effect (hierarchical lithophilicity) induced by Ag nanoparticles and N-doped groups should be illustrated for homogenizing Li deposition and inhibiting the Li dendrite generation. In contrast, NCHSs containing plated Li gradually exhibited an uncontrolled morphology evolution and invalid effect of suppressing dendritic Li (Figure 4e–h). As shown in Figure 4(f) (Li deposition of 1 mAh cm^{-2}), a notable concentrated Li plating on NCHSs appeared, different from the uncycled electrode (Figure 4e). Subsequently, continuous concentrated Li deposition would further cause the morphology deterioration because of the appearance of fatal Li dendrites (Figure 4g). When the plating capacity was 5 mAh cm^{-2} , inevitable development of long Li dendrites occurred on the NCHSs electrode surface (Figure 4h). Although N-doped groups can enhance the coordination with Li ions for lithophilic NCHSs, low utilization of internal space and inadequate outer void are unable to accommodate the volume expansion and limit the growth direction of Li metal, resulting the formation of dendritic Li. For the lithophobic Cu foil, the uncontrollable Li mossy/dendrite could be widely observed even at a low Li capacity of 1 mAh cm^{-2} (Figure S6a) and 3 mAh cm^{-2} (Figure S6b).

The hierarchical lithophilicity strategy endows Ag@NCHSs to inhibit the growth of Li dendrites, which can be further certified by *in-situ* optical microscopy to dynamically explore the morphology variation of the Li plating on the substrate.^[37] Figure 4(i–l) shows the observation results of Li deposition on the NCHSs. Unfortunately, since the NCHSs is unable to

adequately utilize the space inside the cavity, it can only suppress Li dendrites with a small area capacity (Figure 4j). Therefore, during prolonged discharging process, the Li starts to deposit irregularly and eventually some dendrites are formed (Figure 4k and l). Moreover, it is evidently observed that the Li dendrites wildly grew on the bare Cu, raising the risk of short circuit of batteries (Figure S8). Different from the NCHSs, Ag@NCHSs exhibited a contrasting situation during the Li plating process (Figure 4m–p). Profiting from the hierarchical lithophilicity property, uniform and dendrite-free Li nucleation and growth behavior was able to be noticed in the whole plating process of 60 min (5 mAh cm^{-2}).

As exhibited in Figure 5(a), CV measurements between 0.0 and 2.5 V were conducted to verify the generation of Li–Ag alloy sites in Ag@NCHSs, helping induce the preferential internal Li nucleation. During the first cathodic scan, in addition to the LiNO_3 decomposition (1.56 V), three weak peaks located at 0.81 , 0.16 V and 0.03 V should be attributed to the combination of Li ion and N atom, and Li–Ag alloying reaction respectively. In the reverse scan, the appearance of two plateaus at 0.12 and 0.36 V could be significantly observed, which was assigned as a dealloying mechanism.^[38,39] Co-existence of the lithophilic Ag and N-containing groups should be favorable for reducing the deposition barrier. Moreover, to definitely demonstrate the generation of Li–Ag alloy for inducing the preferential Li nucleation and growth, the *in-situ* XRD spectra at Li discharge stage of Ag@NCHSs was collected (Figure 5b), which was measured by a homemade device adopting a pure Be foil as the collector. The clear intensity changes located at 28.2° and 40.3° were favorable for proving the formation of the LiAg phase (JCPDS 04-0805), corresponding to the voltage ranging from 0.3 to 0.0 V (Figure S9). This is well consistent with the CV result in Figure 5a. Interestingly, the gradual disappearance of the LiAg phase (dealloying behavior) and the increased intensity of the Ag phase during the Li charge process could be reasonably observed (Figure S9).^[40] In Figure S10, it could be calculated that the Li nucleation overpotential on the Ag@NCHSs was 10.0 mV , significantly lower than 20.0 mV of NCHSs (Figure S11) and 50.6 mV of bare Cu foil (Figure S12). To further testify the reversibility and cyclic stability of the Li plating/stripping process, Coulombic efficiency (CE) of three obtained collectors were determined in the coin cells with bare Li anodes. Remarkably, the Ag@NCHSs electrode manifested a stable CE plot (average value of 98.32%) for nearly 400 cycles at 1 mA cm^{-2} with 1 mAh cm^{-2} . In contrast, NCHSs and bare Cu foil showed a limited cycle life of ~ 170 and 110 cycles, and then encountered rapid decaying in the subsequent cycles due to the Li dendrite generation and internal electrolyte consumption (Figure 5c). When the current density was increased to a high condition of 3 mA cm^{-2} , Ag@NCHSs still exhibited a relatively superior CE performance over 250 cycles (Figure 5d), while Cu foil showed an unstable CE with dramatic fluctuations after only 40 cycles. When the testing requirement further increased to 5 mA cm^{-2} , the performance of cycle stability exhibited a stable CE of 150 cycles, while the CE of NCHSs and bare Cu foil samples dropped significantly (Figure 5e). Notably, the rate performance

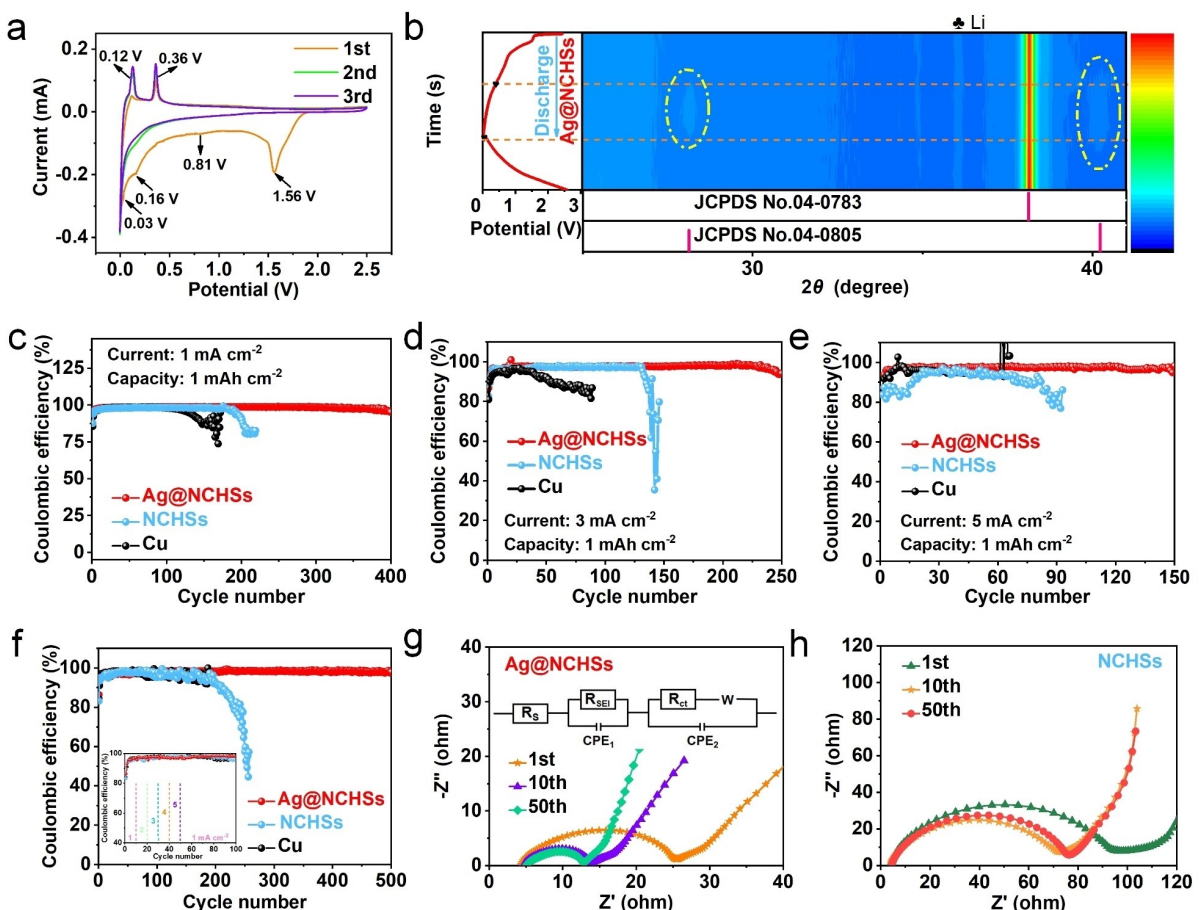


Figure 5. Electrochemical performances of asymmetric cells. a) CV curves of Ag@NCHSs at 0.1 mV s^{-1} . b) In-situ XRD pattern of the Ag@NCHSs electrode and the corresponding discharge plot. CE test of bare Cu foil, NCHSs, and Ag@NCHSs at different current densities of c) 1 mA cm^{-2} , d) 3 mA cm^{-2} and e) 5 mA cm^{-2} for the capacity of 1 mAh cm^{-2} . f) Rate performances of three electrodes. Nyquist plots of g) Ag@NCHSs and h) NCHSs anode after 1, 10 and 50 cycles.

at various current densities strongly demonstrated the significant improvement of CE (Figure 5f). A stable high CE plot for Ag@NCHSs electrode is nearly not influenced by the increased current densities. However, a fluctuated and slowly decayed CE for NCHSs can be observed especially after 100 cycles. Inevitably, bare Cu foil showed a poor retention rate and much bigger fluctuation as an irreversible capacity loss. Furthermore, the Nyquist plots of the asymmetric battery were tested to explore the charge-transfer kinetics and internal resistance after several cycling processes. EIS results of Ag@NCHSs have been fitted by certain EC and the equivalent circuit diagram has also been provided. The obtained EIS and equivalent circuit diagram can reflect the charge and ion transport dynamics of the electrode. Specifically, the semi-circle in EIS spectra refers to the electrochemical charge transfer resistance (R_{ct}) while the intercept with the real impedance axis at high frequency is related to the bulk resistance from liquid electrolytes.^[41] As shown in Figure 5(g), there was an initial resistance of 20.3Ω for the Ag@NCHSs electrode due to the relatively solid interface. Afterwards, gradually stabilized interface, avoided Li dendrites and decreased side reactions ensured the low resistance value below 10Ω after 50 cycles.^[42,43] However, in Figures 5(h) and S13, more inadequate Li stripping from the

substrate and severe SEI accumulation may cause the large initial interface resistance of the NCHSs (85Ω) and Cu electrode (92Ω), compared to the Ag@NCHSs. As expected in the 50th cycle, both NCHSs and Cu electrode still exhibited the poor resistance performance over 70Ω .

The voltage profiles of fabricated symmetric cells loaded with 5 mAh cm^{-2} of Li deposition further exhibit the long-term Li metal transport capability during the galvanostatic charge/discharge process. It is worth mentioning that the Ag@NCHSs@Li electrode displayed a small voltage polarization of 26 mV and exceptional cycling stability (more than 1600 h) without the pronounced voltage fluctuation (Figure 6a). In contrast, compared to Ag@NCHSs@Li electrode, the cell assembled with NCHSs@Li exhibited a larger initial polarization of 42.8 mV , which may be caused by the excess accumulation of interface SEI due to the consumption of fresh Li metal and electrolyte.^[44] The corresponding voltage polarization (VP) values at 1 mA cm^{-2} of Ag@NCHSs@Li and NCHSs@Li-based symmetric cells are presented in Figure 6(b), from which Ag@NCHSs@Li electrode stayed a stable cycling performance for 800 times, much more superior to that (400 cycles) of NCHSs@Li. In addition, the long-term and low VP below 30 mV could further indicate the excellent interface stability of Ag@NCHSs@Li.

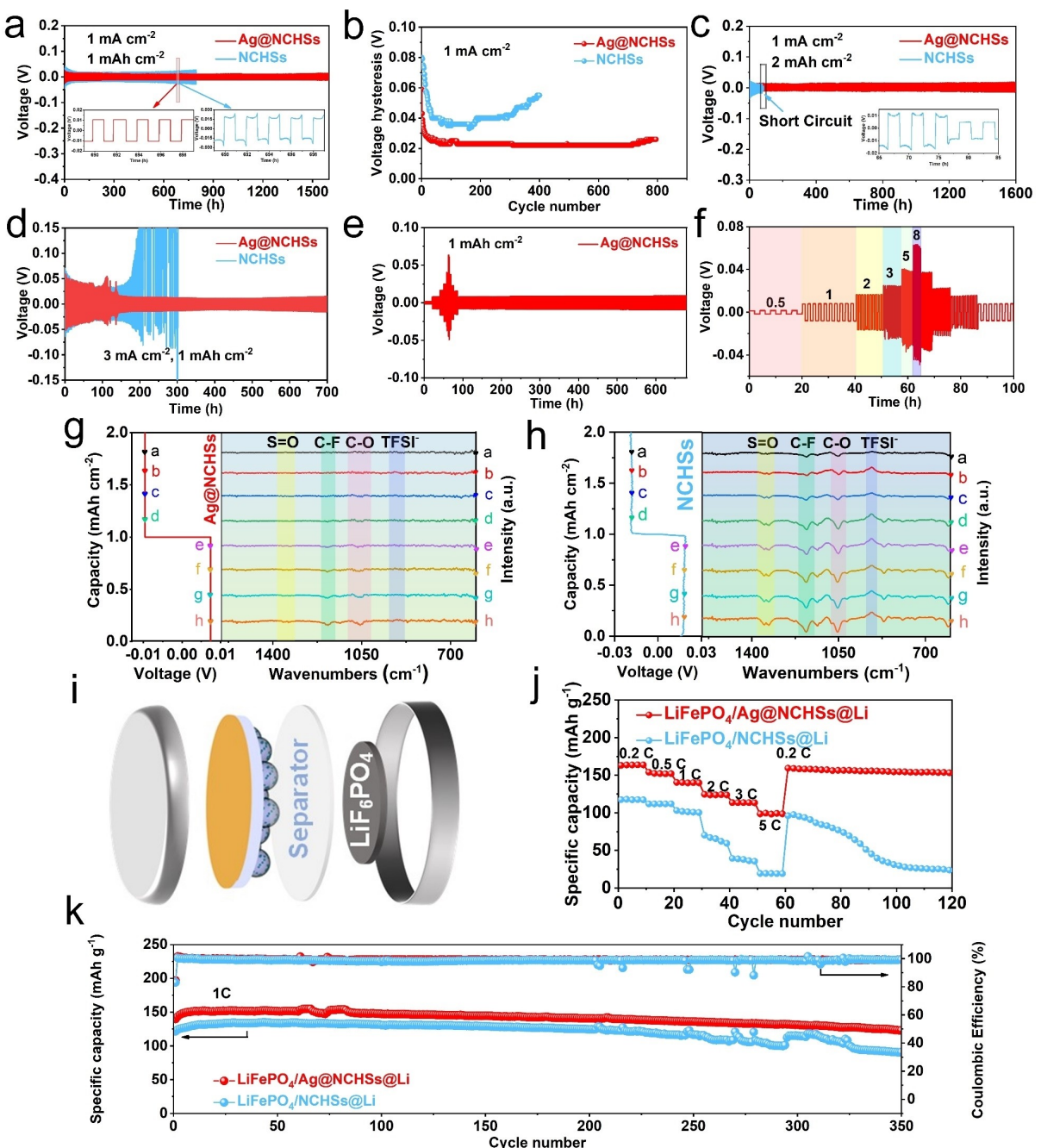


Figure 6. Electrochemical performances of symmetric cells and full cells. Voltage-time profiles of the symmetrical cells using Ag@NCHSS@Li and NCHSS@Li composite anodes at a) 1 mA cm^{-2} and d) 3 mA cm^{-2} with 1 mAh cm^{-2} . b) Voltage hysteresis for Ag@NCHSS@Li and NCHSS@Li electrodes at 1 mA cm^{-2} . c) Voltage-time profiles of the symmetrical cells at 1 mA cm^{-2} with the Li deposition of 2 mAh cm^{-2} . e) Rate performance of the Ag@NCHSS anode at current densities of $0.5, 1, 2, 3, 5, 8 \text{ mA cm}^{-2}$ with a fixed capacity of 5 mAh cm^{-2} and f) the first 100 h voltage profiles. *In-situ* FTIR transmittance spectra of g) Ag@NCHSS and h) NCHSS on electrolyte consumption versus the increased Li deposition capacities. i) Schematic diagram of $\text{LiFePO}_4/\text{Ag@NCHSS@Li}$ full battery assembly. j) Rate performance of $\text{LiFePO}_4/\text{Ag@NCHSS@Li}$ and $\text{LiFePO}_4/\text{NCHSS@Li}$ full cells. k) Discharge capacity and galvanostatic cycling performance of the LiFePO_4 cells at 1 C .

When cycled at a increased capacity of Li plating/stripping, Ag@NCHSS@Li still displayed a superior performance of 1600 h with a stable VP, reflecting the great suppression of fatal Li dendrites (Figure 6c). As shown in Figures S14(a) and S15(a), the enlarged images of voltage plots at 1 mA cm^{-2} with 1 or 2 mAh cm^{-2} are presented. Specially, the cell with Ag@NCHSS exhibited the voltage hysteresis of more than 25 (1 mAh cm^{-2})

and 30 mV (2 mAh cm^{-2}) respectively, much higher than that ($<10 \text{ mV}$) in a short-circuit state. This indicates the symmetric cell stably work without internal short-circuit. Moreover, EIS tests have also been conducted and the corresponding results are displayed in Figures S14(b) and S15(b), in which comparatively high charge transfer resistance can further manifest the nonexistent short circuit. Similarly, even at a high current

density of 3 mA cm^{-2} , Ag@NCHSs@Li also showed a prominent cycling stability for 700 h. It should be noticed that the polarization voltage significantly fluctuated in the initial 100 h. During the Li plating/stripping process at high current density ($> 3 \text{ mA cm}^{-2}$), incomplete Li metal transfer and a little interface residual are inevitable, resulting in the partial SEI accumulation. Consequently, accumulated SEI hinders the quick mass and charge transfer process, inducing the increased voltage polarization. Afterwards, with the development of gradually homogenized electrode interface, stable cycling performance would occur again. For the NCHSs@Li under the same test condition, there was an extremely sharp fluctuation of the voltage-time profiles after 150 h, demonstrating a more severe Li dendrite growth and dead Li generation (Figure 6d). Moreover, the rate capability was conducted by Ag@NCHSs@Li and displayed in Figure 6(e and f). Impressively, Ag@NCHSs@Li delivered the low VP values of 8, 16, 25, 40, and 60 mV from 0.5 to 8 mA cm^{-2} , much better than corresponded VP (47, 93, 140, 226, and 340 mV) of NCHSs@Li (Figure S16). As shown in Figure 6(g), the *in-situ* FT-IR spectroscopy of the cell with Ag@NCHSs@Li electrodes manifested the stable interface to defend the electrolyte corrosion and avoid the side reactions. *In-situ* FT-IR results could be obtained from the sample reflection mode (Attenuated Total Reflection, ATR mode). Figure S17(a) exhibits the testing device for *in-situ* FT-IR measurement, in which the device is placed on the optical system. For collecting the results, three steps should be followed. Specially, as displayed in Figure S17(b), the detection infrared beam reaches the electrode, and the detector collects the beam carrying some information and then analyzed. For these spectra, the upward trend indicates the consumption of original functional groups and the downward trend indicates the formation of new functional groups. Clearly, during the continuous Li deposition/dissolution, negligible change could be obtained from the *in-situ* FT-IR results. In sharp contrast, Figure 6(h) actually reflects the pronounced interaction between the NCHSs@Li and electrolyte. It was apparently observed that the peak intensity around 916 cm^{-1} decreased, assigned to the degradation of the TFSI^- component. Typically, the consumption of TFSI^- should be caused by the electrochemical reduction of electrolyte and Li metal for the additional SEI formation.^[45] Meanwhile, three other broad bands located at 1054 cm^{-1} (C–O groups), 1180 cm^{-1} (C–F groups) and 1340 cm^{-1} (S=O groups) were all correspondingly increased in terms of intensity.^[46–48] The change further indicates the difficult prevention of Li dendrites and unstable electrode interface of NCHSs@Li.

To examine the practicality of Ag@NCHSs in the full cell, the assembled cell with LiFePO_4 cathode was measured and its schematic diagram of cell composition was also exhibited in Figure 6(i). Specially, approximately 5 mAh cm^{-2} of Li metal was plated in the Ag@NCHSs material and acted as the anode. As shown in Figure 6(j), rate performance was conducted and applied to compare the significant difference between Ag@NCHSs and NCHSs current collector. Encouragingly, at the various test conditions, the Ag@NCHSs-based cell exhibited an average reversible capacity of 163.5 (0.2 C), 152.5 (0.5 C), 140.1 (1 C), 124.0 (2 C), 113.5 (3 C) and 98.8 mAh g^{-1} (5 C) respectively,

superior to those of NCHSs@Li-based cell. In addition, it is also necessary for one practical full cell to inspect the long-term charge/discharge behavior. Remarkably, when cycled at 1 C, Ag@NCHSs-based cell delivered a high initial capacity of 139.7 mAh g^{-1} , and then increased to a maximum of 154.7 mAh g^{-1} at the 65th cycle (Figure 6k). Meanwhile, it also delivered a steady CE of nearly 100% and slow capacity decay (123.2 mAh g^{-1} after 350 cycles). By contrast, because of the rapidly producing dead Li, NCHSs only maintained a low capacity of 90.3 mAh g^{-1} after 350 cycles. As illustrated in Figure S18(a and b), the polarization values for the Ag@NCHSs-based cell slowly increased from 123 mV (1st cycle) to 230 mV (350th cycle). However, the cell with NCHSs encountered a rapid increase rate for voltage polarization, which were 180 mV at 1st cycle and 403 mV at 350th cycle respectively (Figure S19a and b). Stable electrode interface is extremely important for eliminating the effect of Li dendrites and avoiding the disadvantage of electrolyte depletion. For the Ag@NCHSs, hierarchical lithiophilicity can effectively ensure the more uniform Li plating/stripping process, which is beneficial to suppressing side reactions and improving the cycling performance.

Conclusion

In summary, unique Ag@NCHSs with the hierarchical lithiophilicity has been proposed as the lithiophilic host for the dendrite-free Li metal anode. Due to the excellent positive effect of interiros Ag component, Li metal is preferentially plated in the internal space and then uniformly dispersed outside of the N-doped hollow carbon spheres, resulting in a model of inside-outside Li deposition. Benefiting from the synergistic effect of the hierarchical lithiophilic sites, dendrite-free Li plating and reduced side reactions can be achieved in Ag@NCHSs substrate, evidenced by *in-situ* optical observation, XRD and FT-IR spectra. Moreover, the Ag@NCHSs electrode delivers an excellent cycling stability over 1600 h without the negligible voltage fluctuation. Superior rate capability and long-term cycling performance can be also exhibited in the Ag@NCHSs-based full cell with the LiFePO_4 cathode. The rational structure design brings a new light to explore stable Li metal anode possessing with the controlled uniform Li deposition.

Experimental Section

Materials

Tetraethylorthosilicate (TEOS), ethanol, cetyltrimethylammonium bromide (CTAB), ammonia solution (25 wt%) and hydrochloric acid solution (37 wt%) were purchased from Sinopharm Chemical Reagent Co., Ltd. Silver nitrate (AgNO_3 , Aldrich), n-butylamine, acetonitrile was obtained from Aladdin Co., Ltd. All the chemicals mentioned above were used as received.

Material synthesis

The preparation of mesoporous silica hollow nanospheres (MHSiO_2) was based on the following steps. Firstly, cetyltrimethylammonium bromide (0.15 g) was dissolved in ethanol aqueous solution containing concentrated ammonia water (25%, 1 mL). The amount of water and ethanol was chosen at 50 mL and 30 mL respectively. Ethyl orthosilicate (1 mL) was put slowly into the above solution, and then the mixture was stirred for 24 h at 35°C. The obtained white flocs were washed with glycol, dispersed in deionized water (160 mL) after centrifugation and then aged for 48 h at 90°C. Subsequently, the obtained product was washed with ethanol, dispersed in the ethanol solution containing concentrated hydrochloric acid (37%, 240 μL), stirred for 3 h at 60°C and centrifuged for collection. Ag-coated MHSiO_2 ($\text{MHSiO}_2@\text{Ag}$) material was obtained by a one-pot reduction process in the presence of alkylamine as described earlier.^[49] 0.05 g MHSiO_2 was added into a propylene reactor containing ethanol (20 mL) at 50°C. Subsequently, 0.025 g of silver nitrate (AgNO_3 , Aldrich) and 20 μL of n-butylamine (Aldrich) were simultaneously added to the above solution and stirred for 15 min. To remove excess Ag precursors, the synthesized $\text{MHSiO}_2@\text{Ag}$ material should be rinsed with ethanol, and then dried at 80°C for 12 h in a vacuum oven. The chemical vapor deposition (CVD) was conducted by placing the $\text{MHSiO}_2@\text{Ag}$ in a quartz boat. Meanwhile, when the heating temperature reached 900°C, a flow of N_2 carrying acetonitrile component (300 mL min^{-1}) was provided and kept for 1 h for the nitrogen-doped graphene coating on the $\text{MHSiO}_2@\text{Ag}$ ($\text{MHSiO}_2@\text{Ag@NC}$). Finally, $\text{MHSiO}_2@\text{Ag@NC}$ could be etched by the mixture solution with HF (10 wt%) overnight to remove mesoporous silica and obtain the Ag@NCHSs .

Material characterizations

SEM (Hitachi SU1510) and TEM (JEOL JEM-200CX, JEM 2100F) were adopted to illuminate the morphologies of Ag@NCHSs and NCHSs . The crystal phases of these prepared samples were carried out by XRD on Rigaku D/max-2550 V at a scan rate of 8 $^\circ\text{C min}^{-1}$. TGA was performed on thermal analyzer Netzsch STA 409 PG/PC in O_2 . BET surface area and pore size distribution of the samples should be measured on Micromeritics ASAP 2020 M+C analyzer. Raman spectra could be acquired by Renishaw inVia Plus with a wavelength of 532 nm. *In-situ* optical microscopy showing Li deposition process was determined by Zeiss Smartzoom 5. *In-situ* XRD test was also conducted by a homemade device to demonstrate the evolution of lithophilic Ag sites for generating the Li–Ag alloy in the Li stripping/plating process. *In-situ* FTIR spectroscopy could be obtained by Nicolet iS50 FT-IR instrument connecting with LAND-CT2001 test system at room temperature.

Electrochemical measurements

The Ag@NCHSs electrodes were made through the typical slurry-coating process. Ag@NCHSs (80 wt%), PVDF (10 wt%), and carbon black (10 wt%) were completely mixed, and strongly stirred in N-methyl pyrrolidone (NMP, Aldrich) overnight to form a slurry with a typical amount of 0.1 g mL^{-1} (Ag@NCHSs/NMP). Afterwards, the slurry was coated onto a cleaned Cu current collector. The electrodes were dried in a vacuum oven at 60°C overnight. Celgard 2400 separator was placed in CR2032 coin cells inside an Ar-filled glovebox (H_2O and O_2 were strictly controlled below 0.1 ppm). 1 M LiTFSI dissolved in DOL/DME (1:1, v/v) and 0.2 M LiNO_3 additive was served as the electrolyte for symmetric and asymmetric cells and an amount of ~40 μL for each cell was fixed. LAND-CT2001 test system was applied to test the Coulombic efficiency and voltage-time profiles. LiFePO_4 cathode was assembled by mixing

LiFePO_4 , PVDF, and acetylene black with a specific ratio (8:1:1, m/m) in NMP. The slurry was dispersed on the Al foil and then dried. The prepared cathode foils loaded with 6 mg cm^{-2} of LiFePO_4 were punched into disks as the size of 12 mm in diameter. Moreover, 1 M LiPF_6 dissolved in EC/DEC (1:1 w/w) was served as electrolyte for full cell and controlled at ~40 μL . The full cells were cycled from 2.5 to 4.2 V at 1 C (1 C = 169 mA g^{-1}). EIS and CV results were collected by CHI760E (Shanghai Chenhua Instrument). For the EIS test, the frequency from 10⁻² to 10⁵ Hz was applied.

Supporting Information

Supporting Information is available from the Wiley Online Library or from the author.

Acknowledgements

X.-M. Lu and T. C. Liu contributed equally to this work. This work is supported by Natural Science Foundation of Shanghai (22ZR1422800), Shanghai Municipal Education Commission (Innovation Program (QD2019008), National Natural Science Foundation of China (52073170), Innovation Program of Shanghai Municipal Education Commission (2019-01-07-00-09-E00021) and Innovative Research Team of High-level Local Universities in Shanghai.

Conflict of Interest

The authors declare no conflict of interest.

Data Availability Statement

The data that support the findings of this study are available from the corresponding author upon reasonable request.

Keywords: chemical vapor deposition • hierarchical lithophilicity • *in-situ* optical microscopy • inside-outside Li deposition • Li metal anode

- [1] J. M. Tarascon, M. Armand, *Nature* **2001**, *414*, 359–367.
- [2] X. Shen, X.-Q. Zhang, F. Ding, J.-Q. Huang, R. Xu, X. Chen, C. Yan, F.-Y. Su, C.-M. Chen, X. Liu, Q. Zhang, *Energy Mater. Adv.* **2021**, *2021*, 1205324.
- [3] J. Liu, Z. N. Bao, Y. Cui, E. J. Dufek, J. B. Goodenough, P. Khalifah, Q. Y. Li, B. Y. Liaw, P. Liu, A. Manthiram, Y. S. Meng, V. R. Subramanian, M. F. Toney, V. V. Viswanathan, M. S. Whittingham, J. Xiao, W. Xu, J. H. Yang, X. Q. Yang, J. G. Zhang, *Nat. Energy* **2019**, *4*, 180–186.
- [4] M. D. Tikekar, S. Choudhury, Z. Y. Tu, L. A. Archer, *Nat. Energy* **2016**, *1*, 1–7.
- [5] Y. Y. Lu, Z. Y. Tu, L. A. Archer, *Nat. Mater.* **2014**, *13*, 961–969.
- [6] D. C. Lin, Y. Y. Liu, Y. Cui, *Nat. Nanotechnol.* **2017**, *12*, 194–206.
- [7] W. Xu, J. L. Wang, F. Ding, X. Chen, E. Nasybulin, Y. H. Zhang, J. G. Zhang, *Energy Environ. Sci.* **2014**, *7*, 513–537.
- [8] K. Xu, *Chem. Rev.* **2014**, *114*, 11503–11618.
- [9] Y. F. Zhang, Y. R. Zhong, S. Q. Liang, B. Wang, X. Chen, H. Wang, *ACS Mater. Lett.* **2019**, *1*, 254–259.

- [10] F. H. Guo, C. Wu, S. L. Chen, X. P. Ai, F. P. Zhong, H. X. Yang, J. F. Qian, *ACS Mater. Lett.* **2020**, *2*, 358–366.
- [11] Y. Cheng, J. Chen, Y. Chen, X. Ke, J. Li, Y. Yang, Z. Shi, *Energy Storage Mater.* **2021**, *38*, 276–298.
- [12] F. Wu, Y.-X. Yuan, X.-B. Cheng, Y. Bai, Y. Li, C. Wu, Q. Zhang, *Energy Storage Mater.* **2018**, *15*, 148–170.
- [13] L. F. Xiao, Z. Q. Zeng, X. W. Liu, Y. J. Fang, X. J. Jiang, Y. Y. Shao, L. Zhuang, X. P. Ai, H. X. Yang, Y. L. Cao, J. Liu, *ACS Energy Lett.* **2019**, *4*, 483–488.
- [14] X. D. Ren, P. Y. Gao, L. F. Zou, S. H. Jiao, X. Cao, X. H. Zhang, H. Jia, M. H. Engelhard, B. E. Matthews, H. P. Wu, H. Lee, C. J. Niu, C. M. Wang, B. W. Arey, J. Xiao, J. Liu, J. G. Zhang, W. Xu, *Proc. Natl. Acad. Sci. USA* **2020**, *117*, 28603–28613.
- [15] S. H. Lee, J. Y. Hwang, J. Ming, Z. Cao, H. A. Nguyen, H. G. Jung, J. Kim, Y. K. Sun, *Adv. Energy Mater.* **2020**, *10*, 2000567.
- [16] Z. Liang, D. C. Lin, J. Zhao, Z. D. Lu, Y. Y. Liu, C. Liu, Y. Y. Lu, H. T. Wang, K. Yan, X. Y. Tao, Y. Cui, *Proc. Natl. Acad. Sci. USA* **2016**, *113*, 2862–2867.
- [17] D. C. Lin, J. Zhao, J. Sun, H. B. Yao, Y. Y. Liu, K. Yan, Y. Cui, *Proc. Natl. Acad. Sci. USA* **2017**, *114*, 4613–4618.
- [18] L. Liu, Y.-X. Yin, J.-Y. Li, N.-W. Li, X.-X. Zeng, H. Ye, Y.-G. Guo, L. J. Wan, *Joule* **2017**, *1*, 563–575.
- [19] T. T. Zuo, X. W. Wu, C. P. Yang, Y. X. Yin, H. Ye, N. W. Li, Y. G. Guo, *Adv. Mater.* **2017**, *29*, 1700389.
- [20] Z. L. Hu, Z. Z. Li, Z. Xia, T. Jiang, G. L. Wang, J. Y. Sun, P. F. Sun, C. L. Yan, L. Zhang, *Energy Storage Mater.* **2019**, *22*, 29–39.
- [21] Y. Yuan, F. Wu, Y. Bai, Y. Li, G. Chen, Z. Wang, C. Wu, *Energy Storage Mater.* **2019**, *16*, 411–418.
- [22] N. W. Li, Y. X. Yin, C. P. Yang, Y. G. Guo, *Adv. Mater.* **2016**, *28*, 1853–1858.
- [23] Y. Liu, D. Lin, P. Y. Yuen, K. Liu, J. Xie, R. H. Dauskardt, Y. Cui, *Adv. Mater.* **2017**, *29*, 1605531.
- [24] S. F. Liu, X. Ji, N. Piao, J. Chen, N. Eidson, J. J. Xu, P. F. Wang, L. Chen, J. X. Zhang, T. Deng, S. Hou, T. Jin, H. L. Wan, J. R. Li, J. P. Tu, C. S. Wang, *Angew. Chem. Int. Ed.* **2021**, *60*, 3661–3671; *Angew. Chem.* **2021**, *133*, 3705–3715.
- [25] Y. Cheng, X. Ke, Y. Chen, X. Huang, Z. Shi, Z. Guo, *Nano Energy* **2019**, *63*, 103854.
- [26] Y. Chen, X. Ke, Y. Cheng, M. Fan, W. Wu, X. Huang, Y. Liang, Y. Zhong, Z. Ao, Y. Lai, G. Wang, Z. Shi, *Energy Storage Mater.* **2020**, *26*, 56–64.
- [27] X. Ke, Y. Cheng, J. Liu, L. Liu, N. Wang, J. Liu, C. Zhi, Z. Shi, Z. Guo, *ACS Appl. Mater. Interfaces* **2018**, *10*, 13552–13561.
- [28] Y. Liang, Y. Chen, X. Ke, Z. Zhang, W. Wu, G. Lin, Z. Zhou, Z. Shi, *J. Mater. Chem. A* **2020**, *8*, 18094–18105.
- [29] X. Ke, Y. Liang, L. Ou, H. Liu, Y. Chen, W. Wu, Y. Cheng, Z. Guo, Y. Lai, P. Liu, Z. Shi, *Energy Storage Mater.* **2019**, *23*, 547–555.
- [30] W. H. Sim, H. M. Jeong, *Adv. Sci.* **2021**, *8*, 2002144.
- [31] K. Yan, Z. D. Lu, H.-W. Lee, F. Xiong, P.-C. Hsu, Y. Z. Li, J. Zhao, S. Chu, Y. Cui, *Nat. Energy* **2016**, *1*, 16010.
- [32] C. P. Yang, Y. G. Yao, S. M. He, H. Xie, E. Hitz, L. B. Hu, *Adv. Mater.* **2017**, *29*, 1702714.
- [33] F.-H. Du, B. Li, W. Fu, Y. J. Xiong, K. X. Wang, J. S. Chen, *Adv. Mater.* **2014**, *26*, 6145–6150.
- [34] X. Huang, H. Yu, H. T. Tan, J. X. Zhu, W. Y. Zhang, C. Y. Wang, J. Zhang, Y. X. Wang, Y. B. Lv, Z. Zeng, D. Y. Liu, J. Ding, Q. C. Zhang, M. Srinivasan, P. M. Ajayan, H. H. Hng, Q. Y. Yan, *Adv. Funct. Mater.* **2014**, *24*, 6516–6523.
- [35] X. J. Liu, M. Xu, J. L. Hu, Y. Li, Q. S. Li, Y. Z. Lu, F. P. Wang, *Adv. Mater. Res.* **2014**, *924*, 319–322.
- [36] W. B. Ye, F. Pei, X. N. Lan, Y. Cheng, X. L. Fang, Q. B. Zhang, N. F. Zheng, D. L. Peng, M. S. Wang, *Adv. Energy Mater.* **2020**, *10*, 1902956.
- [37] T. C. Liu, J. X. Ge, Y. Xu, L. P. Lv, W. W. Sun, Y. Wang, *Energy Storage Mater.* **2020**, *32*, 261–271.
- [38] J. Morales, L. Sanchez, F. Martin, J. R. Ramos-Barrado, M. Sanchez, *J. Electrochem. Soc.* **2004**, *151*, A151–A157.
- [39] M. Fan, B. Chen, K. Wang, Q. Yu, Y. Ding, Z. Lei, F. Liu, Y. Shen, G. He, *Mater. Today* **2021**, *21*, 100751.
- [40] G. Taillades, J. Sarradin, *J. Power Sources* **2004**, *125*, 199–205.
- [41] K. Zhang, F. Wu, K. Zhang, S. Weng, X. Wang, M. Gao, Y. Sun, D. Cao, Y. Bai, H. Xu, X. Wang, C. Wu, *Energy Storage Mater.* **2021**, *41*, 485–494.
- [42] Q. Li, S. P. Zhu, Y. Y. Lu, *Adv. Funct. Mater.* **2017**, *27*, 1606422.
- [43] Q. Q. Qin, N. P. Deng, L. Y. Wang, L. T. Zhang, Y. R. Jia, Z. Dai, Y. Liu, W. M. Kang, B. Cheng, *Chem. Eng. J.* **2019**, *360*, 900–911.
- [44] L. Liu, Y. X. Yin, J. Y. Li, S. H. Wang, Y. G. Guo, L. J. Wan, *Adv. Mater.* **2018**, *30*, 1706216.
- [45] B. D. Adams, E. V. Carino, J. G. Connell, K. S. Han, R. Cao, J. Chen, J. Zheng, Q. Li, K. T. Mueller, W. A. Henderson, J. G. Zhang, *Nano Energy* **2017**, *40*, 607–617.
- [46] D. Aurbach, E. Pollak, R. Elazari, G. Salitra, C. S. Kelley, J. Affinito, *J. Electrochem. Soc.* **2009**, *156*, A694–A702.
- [47] D. Aurbach, I. Weissman, A. Zaban, O. Chusid, *Electrochim. Acta* **1994**, *39*, 51–71.
- [48] D. Aurbach, O. Chusid, I. Weissman, P. Dan, *Electrochim. Acta* **1996**, *41*, 747–760.
- [49] S. Yoo, J. I. Lee, S. Ko, S. Park, *Nano Energy* **2013**, *2*, 1271–1278.

Manuscript received: March 10, 2022

Revised manuscript received: April 4, 2022

Accepted manuscript online: April 6, 2022

Version of record online: April 25, 2022